

Incommensurability enabled quasi-fractal order in 1D narrow-band moiré systems

Miguel Gonçalves,¹ Bruno Amorim,² Flavio Riche,¹ Eduardo V. Castro,^{3,4} and Pedro Ribeiro^{1,4}

¹*CeFEMA-LaPMET, Departamento de Física, Instituto Superior Técnico, Universidade de Lisboa, Av. Rovisco Pais, 1049-001 Lisboa, Portugal*

²*Centro de Física das Universidades do Minho e do Porto (CF-UM-UP), Laboratório de Física para Materiais e Tecnologias Emergentes (LaPMET), Universidade do Minho, Campus de Gualtar, 4710-057 Braga, Portugal*

³*Centro de Física das Universidades do Minho e Porto, Departamento de Física e Astronomia, Faculdade de Ciências, Universidade do Porto, 4169-007 Porto, Portugal*

⁴*Beijing Computational Science Research Center, Beijing 100193, China*

We demonstrate that quasiperiodicity can radically change the ground state properties of 1D moiré systems with respect to their periodic counterparts. By studying an illustrative example we show that while narrow bands play a significant role in enhancing interactions both for commensurate and incommensurate structures, only quasiperiodicity is able to extend the ordered phase down to an infinitesimal interaction strength. In this regime, the quasiperiodic-enabled state has contributions from infinitely many wave vectors. This quasi-fractal regime cannot be stabilized in the commensurate case even in the presence of a narrow band. These findings suggest that quasiperiodicity may be a critical factor in stabilizing non-trivial ordered phases in interacting moiré structures and signal out multifractal non-interacting phases, recently found in 2D incommensurate moiré systems, as particularly promising parent states.

Quasiperiodic structures (QPS) exhibit a plethora of intriguing features, such as non-trivial localization [1–17], multifractality [18–24], and topological [25–31] properties, that can be encountered in diverse settings, including optical lattices [2, 4, 5, 15–17, 32–35], photonics, [3, 12, 25, 27, 36, 37] phononics [38–43], and two-dimensional (2D) moiré materials [44, 45].

Another notable feature of QPS is the formation of narrow (nearly flat) bands [44, 45] in the energy spectrum which enhance correlations in the presence of electron-electron interactions. This enhancement mechanism is believed to underlie the abundance of strongly-correlated phases recently observed in moiré materials.

Beyond its impact on the energy spectrum, quasiperiodicity also affects eigenstates. Nevertheless, beyond localization effects, the impact of incommensurability on the eigenstate structure has been traditionally disregarded to explain the physics of moiré materials [44, 45]. However, recent research on twisted bilayer graphene (tBLG) and related 2D models [11, 13, 46] suggests that in the narrow-band regime incommensurability may induce single-particle states to delocalize both in momentum and position space, resulting in sub-ballistic transport. This suggests that the traditional starting point to include interactions within the narrow-band regime that assumes plane wave single-particle states must be revised.

To establish whether quasiperiodicity plays a role in the emergence of correlated phases beyond the creation of narrow bands requires numerically unbiased methods able to take electron-electron interactions into account in large-scale QPS. In 2D, this is notably challenging due to

the lack of efficient numerical tools. In 1D, on the other hand, ground-state properties can be efficiently studied for fairly large system sizes using the density-matrix-renormalization-group (DMRG) technique [47, 48].

Although somehow less rich than their 2D counterparts [10, 11, 49, 50], 1D QPS may also host phases that are neither localized nor ballistic. These so-called critical multifractal states were first identified at localization-ballistic transitions and later shown to exist in extended regions of the phase space. Interestingly, both in 1D quasiperiodic critical phases and in the incommensurate-driven regime found in the narrow band of tBLG's, eigenstates are delocalized in both real and momentum space [18–24]. This suggests that the study of interactions in the 1D setting may provide relevant insights into 2D moiré structures.

With notable exceptions, most studies of interacting 1D QPS focus on infinite-temperature physics and many-body localization phenomena [51–59]. Interestingly, even at infinite temperature, critical multifractal states, emerging out of their non-interacting counterparts, have been recently proposed [60].

Only a few studies address ground-state localization properties [61–67]. Surprisingly, some of these works revealed that interactions may be irrelevant at criticality [64, 67]. However, the stability of extended multifractal critical phases to interactions has not yet been addressed to our knowledge. Furthermore, a comparison of how interactions differ in their effects on phases of commensurate and incommensurate 1D moiré structures is also absent. Understanding these effects from a theoretical standpoint in 1D QPS could shed light on the rich

physics of 2D moiré materials, for which correlated phenomena were recently experimentally reported in strongly quasiperiodic regimes [68]. Experimentally testing these findings would also open new research directions in 1D optical lattices where moiré structures are routinely implemented.

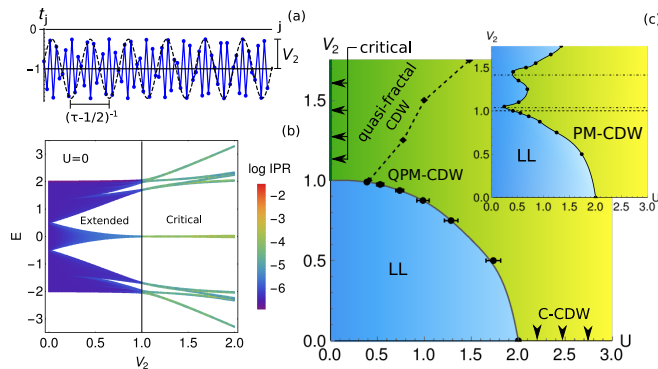


FIG. 1. (a) Hopping modulation for the studied model (see below Eq. 1), with $\tau = 0.5812$. This choice creates a moiré pattern of size $L_M = (\tau - 1/2)^{-1} \approx 12.3$. (b) Single-particle spectrum of the model in the non-interacting limit ($U = 0$) as function of V_2 , for $\tau = 587/1010$ and $N = 1010$ sites, using periodic boundary conditions and $\phi = 0$. $V_2 = 1$ separates phases with extended and critical eigenstates. Each eigenstate is colored according to its inverse participation ratio (IPR) value, defined for a given eigenstate at energy E_n as $\text{IPR}(E_n) = \left(\sum_{i=0}^{N-1} |\psi_i^{(n)}|^4 \right) / \left(\sum_{i=0}^{N-1} |\psi_i^{(n)}|^2 \right)^2$, with $\psi_i^{(n)}$ being the amplitude of the n -th eigenstate at site i . (c) Main figure: Phase diagram of the incommensurate moiré system in the plane of interaction strength U and intensity of quasiperiodic hoppings V_2 , with Luttinger liquid (LL), C-CDW (commensurate CDW) and QPM-CDW (quasiperiodic Moiré CDW) phases. The full and dashed lines connecting the data points are guides to the eye corresponding respectively to a phase transition and a crossover (see text for calculation details). Inset: Phase diagram of a commensurate Moiré system defined by $\tau = \tau_c = 7/12$ and $\phi = 0$, whose exact unit cell is precisely the Moiré pattern. In this case there is a periodic Moiré CDW (PM-CDW) phase at finite V_2 and U . The dashed line is at $V_2 = 1$ and the dot-dashed lines mark points in which the narrow-band's width vanishes in the commensurate case. The lines connecting the data points are guides to the eye.

In this work, we establish that incommensurability may radically change the many-body ground state of a strongly interacting system with respect to similar commensurate structures. Our illustrative example is a 1D tight-binding model that, without interactions, hosts an extended phase of multifractal critical states concomitant with a narrow energy band. Quasiperiodicity is introduced in the modulation of nearest-neighbor hopping [69] with a period close to 2 lattice sites. The ensuing moiré patterns are shown in Fig. 1(a). Fig. 1(b) shows the single-particle band structure of the non-interacting model. A phase transition between an extended (bal-

listic) and a multifractal critical phase arises when the strength of the quasiperiodic modulation, V_2 , reaches $V_2 = 1$. The narrow band centered around zero energy becomes flatter as the critical phase is approached. To target the effect of interactions in the physics of the narrow band, we study the ground-state phase diagram of this model in the presence of nearest-neighbor repulsive interactions, with intensity U , at half-filling, corresponding to a Fermi energy in the middle of the narrow band.

Our main results are summarized in Fig. 1. In the absence of quasiperiodic modulation ($V_2 = 0$) there is a well-known transition from a (gapless) Luttinger Liquid (LL) phase into a (gapped) commensurate CDW (C-CDW) phase with ordering wave-vector $\kappa = \pi$ [70]. For $0 < V_2 < 1$, upon increasing the quasiperiodic modulation, the differences between commensurate and incommensurate systems are not significant up to $V_2 \lesssim 1$: in both cases the LL gapless extended phase is robust up to a finite value of the interaction strength, U . The critical value $U = U_c(V_2)$, beyond which the transition to a gapped CDW phase occurs, decreases with increasing V_2 . We dub this ordered phase, characterized by CDW order with multiple wave vectors, a moiré CDW. Depending on the nature of the system, these additional wave vectors are either commensurate or incommensurate with the lattice. We refer to them as periodic (PM-CDW) or quasiperiodic (QPM-CDW) moiré CDW, respectively.

For $V_2 \geq 1$, commensurate and incommensurate modulations differ drastically once interactions are turned on. For commensurate structures, a gapless LL phase still occurs for small but finite U , transitioning into a gapped PM-CDW phase for larger U . Contrastingly, incommensurability suppresses the LL phase for $V_2 \geq 1$ rendering the system unstable towards a QPM-CDW phase for any finite U . We dub this remarkable QPM-CDW regime arising for small enough values of U and $V_2 \geq 1$ a quasi-fractal CDW due to the quasi-fractal structure of the charge order in this state. As U increases there is a crossover from the quasi-fractal CDW regime into an ordered state similar to the QPM-CDW that occurs for $V_2 < 1$. As we move away from the quasi-fractal regime, the moiré CDW of the incommensurate and commensurate systems becomes increasingly indistinguishable.

The remainder of the paper is organized as follows. After providing details on the model and method, we introduce the different observables tailored to investigate the nature of the CDW phase. We analyze these quantities to infer the impact of interactions in extended and critical states. Finally, we discuss the results and their implications. In the supplemental material (SM) section [71], we provide additional results including a thorough finite scaling analysis that further supports our conclusions.

Model and Methods.— We consider a tight-binding chain of spinless fermions in which the nearest-neighbor hoppings are modulated quasiperiodically [69, 72, 73].

In addition, we take a repulsive interaction of magnitude $U > 0$ between nearest neighbors' densities. The Hamiltonian reads

$$H = \sum_j t_j c_j^\dagger c_{j+1} + \text{h.c.} + U \sum_j n_j n_{j+1} \quad , \quad (1)$$

where c_j^\dagger creates a particle at site j , $t_j = -1 - V_2 \cos[2\pi\tau(j + 1/2) + \phi]$ is the hopping from site $j + 1$ to site j , which has quasiperiodic modulation of strength V_2 and period τ^{-1} . Since j is an integer, if τ is irrational, the periodicity of the hopping term is infinite. In the following we consider the half-filled case, to ensure a gapped ordered state exists at $\kappa = \pi$ for $V_2 = 0$, and open boundary conditions (OBC), that are suitable for the DMRG algorithm (in the SM [71] we present further results for twisted boundary conditions).

Numerical results were obtained with DMRG [47, 48], as implemented in the iTensor library [74, 75]. We required the iTensor's truncation error to be less than 10^{-12} and only stopped the sweeping procedure once convergence requirements are satisfied, up to a maximum of 500 sweeps. In most of the calculations we require the energy variance, $\Delta_H = \langle H^2 \rangle - \langle H \rangle^2$, to be below 10^{-6} ; the ground-state energy difference between two sweeps to be below $\Delta E_{\text{GS}} = 10^{-7}$; and the difference in the entanglement entropy at the middle bond between two sweeps to be below $\Delta S_{\text{GS}} = 10^{-4}$ [76].

For the finite-size scaling analysis, we approximate the irrational τ by a rational number $\tau \simeq \tau_{p,N} = p/N$, and take N to be the size of the chain containing a single unit cell. We then consider a sequence of approximates $\tau_{p,N}$ of increasing size, N .

Throughout the paper we take $\tau = 1/2 + \delta \simeq 1/2$. This choice ensures the formation of a narrow-band at the center of the energy spectrum, as we detail in the SM [71]. The period of the corresponding moiré pattern, $L_m = (\tau - 1/2)^{-1} = \delta^{-1}$, increases as τ approaches $1/2$. At the same time the central narrow-band in Fig. 1 becomes increasingly flat (see [71]), rendering DMRG convergence progressively difficult. For these reasons, we set $\tau \simeq 0.5812$. Furthermore, to decrease finite-size effects when capturing the CDW order for twisted boundary conditions (in the SM [71]), we consider system sizes with an even number of sites. Also, we do not draw approximants from an exact sequence of rational convergents of τ , as this would severely limit the available system sizes. Instead, having in mind that physical properties should not depend on slight variations in τ , we choose rational approximants that are very close to $\tau = 1453/2500 = 0.5812$, which we took to be the largest system size containing $N = 2500$ sites. The particular series of chosen approximants follows,

N	112	198	308	504	1010	1478	2008	2500
$\tau_{p,N}$	$\frac{65}{112}$	$\frac{115}{198}$	$\frac{179}{308}$	$\frac{293}{504}$	$\frac{587}{1010}$	$\frac{859}{1478}$	$\frac{1167}{2008}$	$\frac{1453}{2500}$

We compare the incommensurate (IS) and commensurate systems (CS) where the repeating unit cell is taken to coincide with the moiré pattern wavelength. Concretely, we considered $\tau = \tau_c = 7/12$, corresponding to a unit cell with 12 sites.

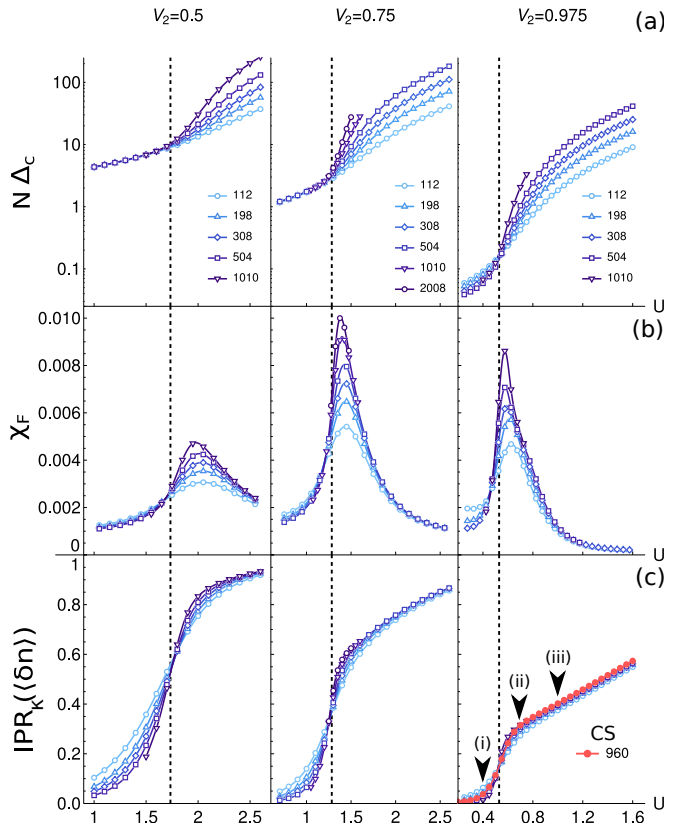


FIG. 2. Finite-size scaling results for: (a) charge gap, Δ_c , defined in Eq. 2; (b) normalized fidelity susceptibility, χ_F , defined in Eq. 3, computed for consecutive $U = U_i$ in (a) and with $\delta U = U_{i+1} - U_i$; (c) $\text{IPR}_k(\langle \delta \mathbf{n} \rangle)$ defined in Eq. 5. The top label indicates the value of V_2 used in the corresponding column (a-c). The dashed lines correspond to the thermodynamic limit extrapolation of the critical point. In (c), results for the CS with $\tau_c = 7/12$ are shown in red, for $\phi = 0$. All other results are for an IS with $\phi = \pi/4$.

For establishing the phase diagram we consider different quantities. The first is the charge gap, which distinguishes between gapped and gapless phases, and is defined as

$$\Delta_c = E(N_p + 1) + E(N_p - 1) - 2E(N_p) \quad (2)$$

where $E(N_p)$ is the ground-state energy for a filling of N_p particles (at half-filling, $N_p = N/2$). In the (gapless) LL phase $\lim_{N \rightarrow \infty} \Delta_c = 0$, while Δ_c approaches a non-zero constant within a gapped CDW phase. To unbiasedly detect quantum phase transitions, we compute the fidelity between ground-states at different values of U , defined as $F = |\langle \Psi(U) | \Psi(U + \delta U) \rangle|$ [77], where $|\Psi(U)\rangle$ denotes

the many-body ground-state for interaction strength U . More concretely, we study the fidelity susceptibility normalized by the system size

$$\chi_F = \frac{-2 \log F}{N \delta U^2}, \quad (3)$$

in the limit $\delta U \rightarrow 0$ [77]. At a quantum phase transitions χ_F diverges as N increases.

We also compute the average density fluctuations given by $\langle \delta n_m \rangle = \langle n_m \rangle - 1/2$, where the expectation value is taken with respect to the ground state, and its discrete Fourier transform:

$$\langle \delta n_\kappa \rangle = \frac{1}{\sqrt{N}} \sum_{m=0}^{N-1} e^{i\kappa m} \langle \delta n_m \rangle \quad (4)$$

where κ takes values $\kappa_j = 2\pi j/N$, $j = 0, \dots, N-1$, which signals the formation of CDW phases. Since the model in Eq. 1 is symmetric under the particle-hole transformation $c_j^\dagger \rightarrow (-1)^j c_j$, we have that $\langle \delta n_m \rangle = 0$ at half-filling. Therefore, in order to detect ordered phases, we add an edge field term to the Hamiltonian of Eq. (1) of the form $\epsilon c_0^\dagger c_0$, setting $\epsilon = 2$. In an ordered phase, the edge field ($\epsilon \neq 0$) selects a particular CDW state, inducing extensive density fluctuations and therefore $\langle \delta n_\kappa \rangle \sim N^{1/2}$, for the κ wave-vectors contributing to the CDW charge fluctuations. In a disordered phase, the edge field only induces non-extensive boundary fluctuations and therefore $\langle \delta n_\kappa \rangle \sim N^{-1/2}$ at any κ . Thus a given wave-vector, κ , is present in the CDW if $K_\kappa = \lim_{N \rightarrow \infty} \langle \delta n_\kappa \rangle / N^{1/2}$ is finite. To quantitatively distinguish between ordered and disordered phases, we define an inverse participation ratio for the charge fluctuations $\langle \delta n_\kappa \rangle$ as

$$\text{IPR}_\kappa(\langle \delta \mathbf{n} \rangle) = \left(\sum_{\kappa=0}^{N-1} |\langle \delta n_\kappa \rangle|^4 \right) / \left(\sum_{\kappa=0}^{N-1} |\langle \delta n_\kappa \rangle|^2 \right)^2. \quad (5)$$

In a disordered phase, there are only boundary fluctuations, implying that $\text{IPR}_\kappa(\langle \delta \mathbf{n} \rangle) \sim N^{-1}$; while in a charge ordered phase there are finite bulk fluctuations for any system size described by a non-extensive number of wave vectors κ , implying that $\text{IPR}_\kappa(\langle \delta \mathbf{n} \rangle) \sim N^0$. For a conventional (commensurate) CDW phase with order only at $\kappa = \pi$, we simply have $\text{IPR}_\kappa(\langle \delta \mathbf{n} \rangle) = 1$. To improve the estimation of the phase transition points, we also considered the entanglement entropy at the middle bond and the squared fluctuations $\chi_R = N^{-1} \sum_i \langle \delta n_i \rangle^2$ (see SM [71]).

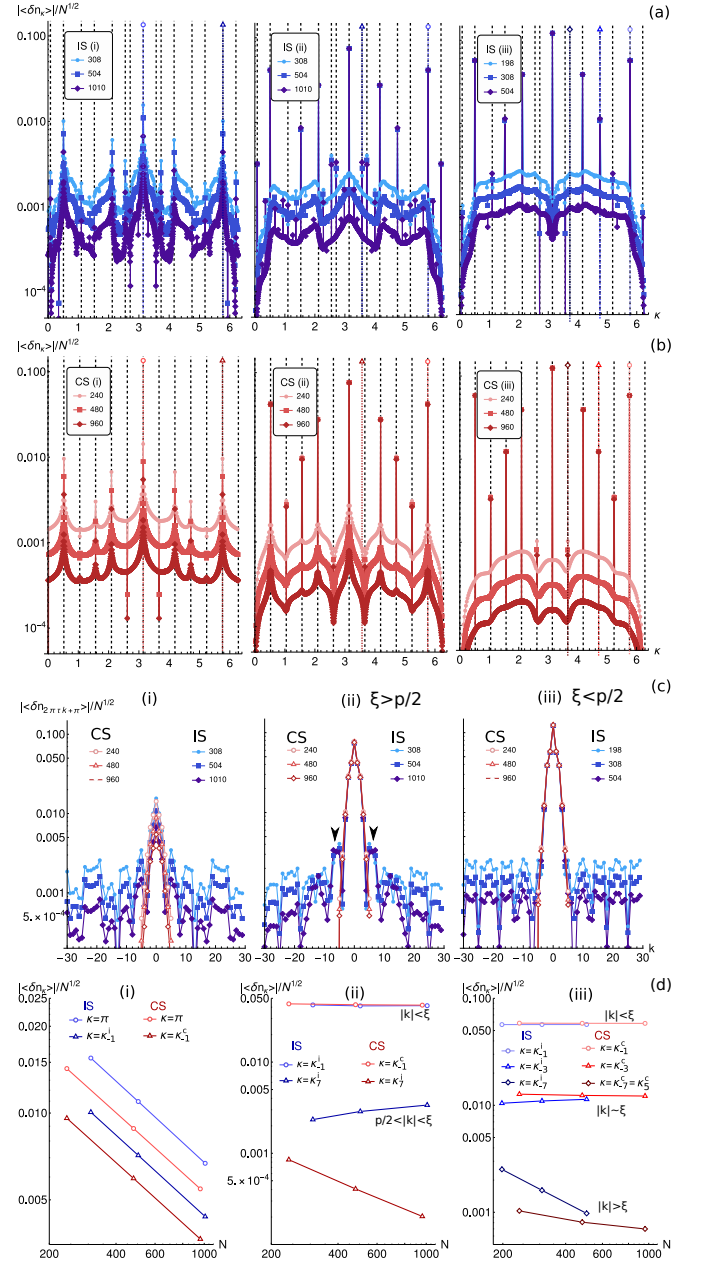


FIG. 3. Fourier transform of charge fluctuations, $|\langle \delta n_\kappa \rangle|/N^{1/2}$, for IS (a) and CS (b), for $V_2 = 0.975$ and for the values of U marked in Fig. 2(d). The dashed lines correspond to $\kappa_k^i = \pi + 2\pi\tau k$, $k = -7, \dots, 7$ in (a) and to $\kappa_k^c = \pi + 2\pi\tau_c k$, $k = -6, \dots, 5$ in (b) - in the latter case, the wave vectors repeat for k outside this interval. (c) $|\langle \delta n_\kappa \rangle|/N^{1/2}$ plotted as a function of the ordering index k . For $\xi > p/2$, the IS has order at wave vectors that are absent in the CS, marked by the arrows in the middle figure. For $\xi < p/2$ on the other hand there is only order at $|k| \lesssim \xi < p/2$ both in the CS and IS. (d) Finite-size scaling for selected peaks, indicated in the legend and by the open markers in (a,b). For $U < U_c(V_2)$ (i), $|\langle \delta n_\kappa \rangle|/N^{1/2} \rightarrow 0$, which implies that $K_\kappa = 0$ for all κ . For $U > U_c(V_2)$, $K_\kappa > 0$ for $|k| \lesssim \xi/2$. For $U \approx U_c(V_2)$ (ii), we can have $\xi > p/2$ in which case K_κ becomes finite for some $|k| > p/2$. An example is shown for $k = 7$, where we see that $K_\kappa > 0$ for $\kappa = \kappa_7^i \neq \kappa_{-5}^i$ for the IS, while no equivalent wave vector exists for the CS since $\kappa_7^c = \kappa_{-5}^c$. In fact we see that $K_\kappa \approx 0$ for $\kappa = \kappa_7^i$ in the CS. For larger U (iii), we see that $K_\kappa > 0$ for $|k| \lesssim \xi < p/2$, while $K_\kappa \approx 0$ for $|k| > \xi$.

To compute the phase transition points in Fig. 1(c), for the incommensurate case, we used a thermodynamic-limit extrapolation of the finite-size results for each computed quantity and estimated the critical point to be the average of the obtained values (see SM [71] for details). For the commensurate case, a thermodynamic-limit extrapolation of the $\text{IPR}_\kappa(\langle\delta\mathbf{n}\rangle)$ results was used to obtain the phase diagram in the inset of Fig. 1(c).

Fate of extended states in the presence of interactions.

— We start by establishing the stability of the (ballistic and gapless) LL state, away from $U = 0$, when interactions are turned on and $V_2 < 1$. This is shown in Figs. 2(a) and (c) where, for $U < U_c(V_2)$, both Δ_c and $\text{IPR}_\kappa(\langle\delta\mathbf{n}\rangle)$ decrease linearly with N . Interestingly, Fig. 2(a) shows that $\lim_{N \rightarrow \infty} N\Delta_c$ decreases rapidly as $V_2 \rightarrow 1$, which we interpret as a many-body signature of the flattening of the dispersion relation observed at in Fig. 1(a) for $U = 0$.

For $U > U_c(V_2)$, the results of Figs. 2(a) and (c) are compatible with $\lim_{N \rightarrow \infty} \Delta_c \neq 0$ and $\lim_{N \rightarrow \infty} \text{IPR}_\kappa(\langle\delta\mathbf{n}\rangle) \neq 0$, i.e. with the existence of a gapped state with CDW order. The LL-CDW phase transition at $U_c(V_2)$ is well captured by the divergence of χ_F with N , shown in Fig. 2(b).

Fig. 2(c)-right panel shows that the stability of the LL phase holds for both CS and IS and that the LL-CDW transition arises for similar $U_c(V_2)$. However, within the CDW we observe a subtle difference between the CS and IS sufficiently close to $U_c(V_2)$.

Fig. 3(c) depicts the normalized Fourier transform of the charge fluctuations $|\langle\delta n_\kappa\rangle|$ for the IS (a) and CS (b), for $V_2 \lesssim 1$. Fig. 3(c) shows the scaling of $|\langle\delta n_\kappa\rangle|/N^{1/2}$ for the some chosen values of the momentum κ .

In the disordered LL phase [case (i)], $K_\kappa = \lim_{N \rightarrow \infty} |\langle\delta n_\kappa\rangle|/N^{1/2}$ vanishes for all κ , whereas for the staggered CDW at $V_2 = 0$ (not shown) $K_{\kappa=\pi} = 1$ and $K_{\kappa \neq \pi} = 0$. For $V_2 > 0$, in the ordered state there are contributions from several κ .

For CS with period p there are p inequivalent contributing wave vectors. For the example of Fig. 3(b), with $\tau = \tau_c = 7/12$, there are $p = 12$ wave vectors, $\kappa_k^c = \pi + 2\pi\tau_c k$ with $k = -6, \dots, 5$ (shown as dashed lines).

For IS, the number of contributing wave vectors increases linearly with N , and we find they are given by $\kappa_k^i = \pi + 2\pi\tau k$, $k = 0, \pm 1, \pm 2, \dots, \pm N/2$.

In Fig. 3(c), the contributions of each wave-vector are ordered by magnitude, $K_{\kappa|k|} > K_{\kappa|k|+1}$. For both IS and CS, $K_{\kappa|k|}$ decreases exponentially with k . i.e. $K_{\kappa|k|} \sim e^{-|k|/\xi}$, where ξ is a characteristic decay-scale that decreases with increasing $U > U_c(V_2)$. Therefore, we may distinguish two cases: $\xi > p/2$ and $\xi < p/2$. For $\xi \ll p/2$, [case (iii) of figure 3(c)] there is no difference between the IS and CS since all relevant contributing wave-vectors have $|k| \lesssim \xi \ll p/2$. On the other hand, for U sufficiently close to $U_c(V_2)$ and V_2 sufficiently close to 1,

we can find a region where $\xi > p/2$ [as illustrated in case (ii) of figure 3(c)]. For this case there are more relevant contributing wave-vectors in IS than for CS and therefore the $\text{IPR}_\kappa(\langle\delta\mathbf{n}\rangle)$ differs for these two cases. Nevertheless the exponential decay of $K_{\kappa|k|}$ ensures $\text{IPR}_\kappa(\langle\delta\mathbf{n}\rangle)$ is finite and qualitatively similar for CS and IS.

As discussed in the methods section, results of Figs. ?? are obtained with DMRG by applying a symmetry-breaking field. In the SM [71], we analyzed the structure factor with no symmetry-breaking while imposing closed boundary conditions. While the available system sizes are significantly smaller, the results seem confirm the findings in the main text (see SM [71]).

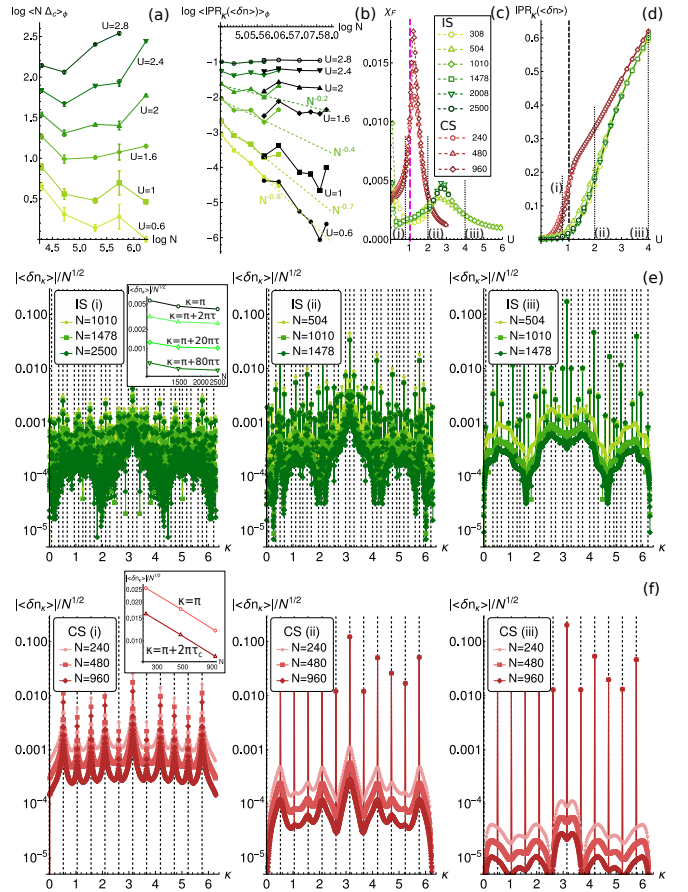


FIG. 4. (a,b) Results after averaging over different configurations of ϕ , for sizes up to $N = 504$, for the IS. Most results were obtained for $N_c = 50$ configurations of ϕ , given by $\phi_i = 2\pi i/N_c$, $i = 0, \dots, N_c - 1$. In black we show results obtained for larger sizes, for fixed $\phi = 1.8$. Dashed lines correspond to linear fits using only the 4 smallest system sizes. (c,d) Results for IS: green, for fixed $\phi = 1.8$ and larger sizes (up to $N = 2500$); CS: red, for fixed $\phi = 0$. The dashed line corresponds to the extrapolated critical point for the CS using the $\text{IPR}_\kappa(\langle\delta\mathbf{n}\rangle)$ results. (e,f) Examples of $|\langle\delta n_\kappa\rangle|/N^{1/2}$ for the U values marked in (c,d) for the IS (e) and the CS (f). The dashed lines correspond to $\kappa = \pi + 2\pi\tau k$, $k \in [-16, 16]$ in (e) and to $\kappa = \pi + 2\pi\tau_c k$, $k \in [-6, 6]$ in (f).

Fate of critical multifractal states in the presence of interactions. — We now turn to the region $V_2 > 1$ that hosts critical multifractal states for $U = 0$. Here, upon increasing U , we find that incommensurability plays a crucial role as CS and IS give rise to radically different physics. This is illustrated in Figs. 4(c) and (d) that show the behavior of χ_F and $\text{IPR}_\kappa(\langle\delta\mathbf{n}\rangle)$. For CS, the finite size scaling of χ_F around $U = U_c \approx 1$ indicates a thermodynamic divergence concomitant with an abrupt change of $\text{IPR}_\kappa(\langle\delta\mathbf{n}\rangle)$. Together with the behavior for the entanglement entropy (see SM [71]), the overall physical picture is similar to that obtained for $V_2 < 1$ — the LL is stable at small U and transitions to a CDW for a critical value of the interactions $U = U_c(V_2)$. Note that for CS with fixed ϕ and $V_2 \geq 1$ there are cases for which hoppings vanish within a unit cell signaling that the narrow-band becomes exactly flat at $U = 0$ (indicated by the dot-dashed lines in the inset of Fig. 1(c), for $\phi = 0$). Although the U_c of the LL-CDW transition is suppressed around these points, it remains finite.

On the other hand, for IS, both χ_F and $\text{IPR}_\kappa(\langle\delta\mathbf{n}\rangle)$ converge everywhere (for the larger system sizes) which suggest no phase transition arises for $U > 0$. Instead, our results point to a crossover, signaled by a peak of χ_F around $U \sim 2.7$, from a regular CDW state at large U to a peculiar CDW — the quasi-fractal CDW — at small U . These results are further corroborated by those in Figs. 4(a) and (b). Fig. 4(a) shows that for larger values of U the average $N\Delta_c$ increases with N (for sufficiently large N) but remains essentially constant for $U \lesssim 1$. In the same way, $\text{IPR}_\kappa(\langle\delta\mathbf{n}\rangle)$ decreases with N for $U \lesssim 1$, as see Fig. 4(b). Note that for $V_2 \gtrsim 1$ there is a dependence on the phase ϕ for the smaller system sizes. For those we average over different configurations of ϕ , while for larger N , when this dependence is small, we only show a typical value of ϕ . The results in Figs. 4(a-d) point to an instability of critical multifractal states, towards a CDW phase with a very small gap and a large number of wave vectors contributing to the charge fluctuations. The quasi-fractal nature of this regime can be seen from the scaling $\text{IPR}_\kappa(\langle\delta\mathbf{n}\rangle) \sim N^{-\alpha}$, $0 < \alpha < 1$ [see fits in Fig. 4(b)].

It is worth noting that in the vicinity of $V_2 = 1$, the flattening of the narrow-band suppresses the charge gap, and makes it impossible to meet the DMRG convergence criteria. This is particularly problematic at small U , where Δ_c takes the smallest values. To circumvent this problem we consider $V_2 = 3.5$ throughout this section, for which we were able to reach DMRG convergence criteria down to $U = 0$ (see SM [71]). Nevertheless, the conclusions above are consistent with the results obtained for smaller values of V_2 (down to $V_2 = 1$) given in the SM [71] for which convergence can be only be achieved for sufficiently large U . Furthermore, the vanishing of the critical interaction strength U_c when the critical regime is reached is also supported by the observed behavior

$U_c(V_2) \sim (1 - V_2)^\mu$, with $\mu \approx 0.4$ for $V_2 < 1$ (see SM [71]).

The characteristic interaction strength where the quasi-fractal CDW crosses over to regular CDW order cannot be defined uniquely. In Fig. 1 (dashed lines), we use the points at which $\partial\text{IPR}_\kappa(\langle\delta\mathbf{n}\rangle)/\partial U$ is maximal. An alternative definition, consisting of maximizing χ_F , yields slightly larger values of U but the same physical picture.

To further illustrate how quasi-fractal CDW order differs from previously known states, we show in Figs. 4(e,f) representative results for $|\langle\delta n_\kappa\rangle|/N^{1/2}$ in IS and CS. For large enough U , there are no significant differences between the type of order observed in IS [see (e-iii)], and CS [see (f-iii)]. In this case $K_{\kappa_{|k|}} \sim e^{-|k|/\xi}$, as for $V_2 < 1$ (further details on the decay are given in the SM [71]).

This picture drastically changes for the IS when U crosses-over to the quasi-fractal regime. Here, the IS order acquires contributions from a large number of wave-vectors as shown in (e-ii) and in the SM [71]. As U decreases within the quasi-fractal regime, ξ increases and rapidly becomes larger than the system size, $\xi \gtrsim N$. This is illustrated in (e-i) where a finite contribution K_{κ_k} is shown to persist up to large $|k|$. Since $\text{IPR}_\kappa(\langle\delta\mathbf{n}\rangle) \rightarrow 0$ as $U \rightarrow 0$, we conjecture that $\xi \rightarrow \infty$ in the limit $U \rightarrow 0$, with all wave-vectors, $\kappa = \kappa_k^i$, contributing for $U = 0^+$.

This is in sharp contrast with CS for which contributions only arise from the p wave-vectors $\kappa = \kappa_k^c$ [see (f-ii)] within the ordered phase. For sufficiently small U , CS enter the disordered phase signaled by the decay of $|\langle\delta n_\kappa\rangle|/N^{1/2}$ with N in (f-i), which implies $K_\kappa = 0$ for all κ .

Discussion.— We determined the ground-state phase diagram of a 1D interacting narrow-band moiré system, at half-filling, which hosts both extended and critical single-particle states. Once interactions are switched on, commensurate (periodic) systems always stabilize the (gapless) Luttinger liquid phase for sufficiently small values of interaction strength, with a transition to a (gapped) periodic moiré CDW state occurring at a finite U value.

Contrastingly, in the incommensurate (quasiperiodic) system the Luttinger liquid phase is suppressed immediately for an infinitesimal interaction strength when the non-interacting states are critical and multifractal. The ensuing ordered phase is a quasi-fractal CDW, characterized by contributions from a large number of wave vectors. Increasing the interaction strength induces a crossover from the quasi-fractal CDW regime, to a regular quasiperiodic moiré regime, in which only a small subset of wave vectors effectively contribute, as in the commensurate case.

These findings demonstrate that quasiperiodicity may radically change the ground state properties of 1D moiré systems with respect to their periodic counterparts. Perhaps our most important result is that, while the narrow

band plays an important role in enhancing interactions both for commensurate and incommensurate structures, only in the quasiperiodic case the ordered phase extends down to infinitesimal interactions, resulting in infinitely many contributing wave vectors. This quasi-factal regime cannot be stabilized in the commensurate case even in the presence of a narrow band.

Our results are a significant first step in understanding the interplay between incommensurability and interactions in moiré systems, clearly demonstrating the need to explicitly consider quasiperiodicity. They also suggest that other critical multifractal phases of non-interacting systems can yield exotic correlated states once interactions are turned on. A particular promising avenue is to study the role of interactions in the recently theoretically reported critical phases of tBLG [11, 13, 46] and in other 2D moiré systems such as twisted trilayer graphene where strong quasiperiodic effects were recently experimentally reported [68], to understand if incommensurability effects can help explain the plethora of exotic phases shown to arise in these systems.

The authors MG and PR acknowledge partial support from Fundação para a Ciência e Tecnologia (FCT-Portugal) through Grant No. UID/CTM/04540/2019. BA and EVC acknowledge partial support from FCT-Portugal through Grant No. UIDB/04650/2020. MG acknowledges further support from FCT-Portugal through the Grant SFRH/BD/145152/2019. BA acknowledges further support from FCT-Portugal through Grant No. CEECIND/02936/2017. Some computations were performed on Tianhe-2JK cluster at the Beijing Computational Science Research Center (CSRC)

-
- [1] S. Aubry and G. André, Proceedings, VIII International Colloquium on Group-Theoretical Methods in Physics **3** (1980).
- [2] G. Roati, C. D’Errico, L. Fallani, M. Fattori, C. Fort, M. Zaccanti, G. Modugno, M. Modugno, and M. Inguscio, *Nature* **453**, 895 (2008), [arXiv:0804.2609](#).
- [3] Y. Lahini, R. Pugatch, F. Pozzi, M. Sorel, R. Morandotti, N. Davidson, and Y. Silberberg, *Physical Review Letters* (2009), [10.1103/PhysRevLett.103.013901](#).
- [4] M. Schreiber, S. S. Hodgman, P. Bordia, H. P. Lüschen, M. H. Fischer, R. Vosk, E. Altman, U. Schneider, and I. Bloch, *Science* **349**, 842 (2015), [arXiv:1501.05661](#).
- [5] H. P. Lüschen, S. Scherg, T. Kohlert, M. Schreiber, P. Bordia, X. Li, S. Das Sarma, and I. Bloch, *Physical Review Letters* (2018), [10.1103/PhysRevLett.120.160404](#).
- [6] D. S. Borgnia, A. Vishwanath, and R.-J. Slager, *Phys. Rev. B* **106**, 054204 (2022).
- [7] C. Huang, F. Ye, X. Chen, Y. V. Kartashov, V. V. Konotop, and L. Torner, *Scientific Reports* **6**, 32546 (2016).
- [8] J. H. Pixley, J. H. Wilson, D. A. Huse, and S. Gopalakrishnan, *Phys. Rev. Lett.* **120**, 207604 (2018).
- [9] M. J. Park, H. S. Kim, and S. Lee, *Phys. Rev. B* **99**, 245401 (2019), [arXiv:1812.09170](#).
- [10] B. Huang and W. V. Liu, *Phys. Rev. B* **100**, 144202 (2019).
- [11] Y. Fu, E. J. König, J. H. Wilson, Y.-Z. Chou, and J. H. Pixley, *npj Quantum Materials* **5**, 71 (2020).
- [12] P. Wang, Y. Zheng, X. Chen, C. Huang, Y. V. Kartashov, L. Torner, V. V. Konotop, and F. Ye, *Nature* (2020), [10.1038/s41586-019-1851-6](#), [arXiv:2009.08131](#).
- [13] M. Gonçalves, H. Z. Olyaei, B. Amorim, R. Mondaini, P. Ribeiro, and E. V. Castro, *2D Materials* **9**, 011001 (2021).
- [14] P. Bordia, H. Lüschen, S. Scherg, S. Gopalakrishnan, M. Knap, U. Schneider, and I. Bloch, *Phys. Rev. X* **7**, 041047 (2017).
- [15] H. Yao, H. Khoudli, L. Bresque, and L. Sanchez-Palencia, *Phys. Rev. Lett.* **123**, 070405 (2019).
- [16] H. Yao, T. Giamarchi, and L. Sanchez-Palencia, *Phys. Rev. Lett.* **125**, 060401 (2020).
- [17] R. Gautier, H. Yao, and L. Sanchez-Palencia, *Phys. Rev. Lett.* **126**, 110401 (2021).
- [18] W. DeGottardi, D. Sen, and S. Vishveshwara, *Phys. Rev. Lett.* **110**, 146404 (2013).
- [19] F. Liu, S. Ghosh, and Y. D. Chong, *Phys. Rev. B - Condens. Matter Mater. Phys.* **91**, 014108 (2015).
- [20] J. Wang, X.-J. Liu, G. Xianlong, and H. Hu, *Phys. Rev. B* **93**, 104504 (2016).
- [21] T. Čadež, R. Mondaini, and P. D. Sacramento, *Physical Review B* (2019), [10.1103/PhysRevB.99.014301](#), [arXiv:1808.10238](#).
- [22] X. Deng, S. Ray, S. Sinha, G. V. Shlyapnikov, and L. Santos, *Phys. Rev. Lett.* **123**, 025301 (2019).
- [23] Y. Wang, L. Zhang, S. Niu, D. Yu, and X.-J. Liu, *Phys. Rev. Lett.* **125**, 073204 (2020).
- [24] T. Liu, X. Xia, S. Longhi, and L. Sanchez-Palencia, *SciPost Phys.* **12**, 27 (2022).
- [25] Y. E. Kraus, Y. Lahini, Z. Ringel, M. Verbin, and O. Zeitlinger, *Physical Review Letters* (2012), [10.1103/PhysRevLett.109.106402](#), [arXiv:1109.5983](#).
- [26] Y. E. Kraus and O. Zeitlinger, *Phys. Rev. Lett.* **109**, 116404 (2012).
- [27] M. Verbin, O. Zeitlinger, Y. E. Kraus, Y. Lahini, and Y. Silberberg, *Physical Review Letters* (2013), [10.1103/PhysRevLett.110.076403](#), [arXiv:1211.4476](#).
- [28] J. L. Lado and O. Zeitlinger, *Phys. Rev. Research* **1**, 033009 (2019).
- [29] O. Zeitlinger, *Opt. Mater. Express* **11**, 1143 (2021).
- [30] D. S. Borgnia and R.-J. Slager, *Phys. Rev. B* **107**, 085111 (2023).
- [31] M. Rösner and J. L. Lado, *Phys. Rev. Research* **3**, 013265 (2021).
- [32] D. J. Boers, B. Goedeke, D. Hinrichs, and M. Holthaus, *Phys. Rev. A* **75**, 63404 (2007).
- [33] M. Modugno, *New Journal of Physics* **11**, 33023 (2009).
- [34] F. A. An, K. Padavić, E. J. Meier, S. Hegde, S. Ganeshan, J. H. Pixley, S. Vishveshwara, and B. Gadway, *Phys. Rev. Lett.* **126**, 040603 (2021).
- [35] T. Kohlert, S. Scherg, X. Li, H. P. Lüschen, S. Das Sarma, I. Bloch, and M. Aidelsburger, *Phys. Rev. Lett.* **122**, 170403 (2019).
- [36] M. Verbin, O. Zeitlinger, Y. Lahini, Y. E. Kraus, and Y. Silberberg, *Phys. Rev. B* **91**, 64201 (2015).
- [37] A. D. Sinelnik, I. I. Shishkin, X. Yu, K. B. Samusev, P. A. Belov, M. F. Limonov, P. Ginzburg, and M. V.

- Rybin, *Advanced Optical Materials* **8**, 2001170 (2020), <https://onlinelibrary.wiley.com/doi/pdf/10.1002/adom.202001170>
- [38] D. J. Apigo, W. Cheng, K. F. Dobiszewski, E. Prodan, and C. Prodan, *Phys. Rev. Lett.* **122**, 095501 (2019).
- [39] X. Ni, K. Chen, M. Weiner, D. J. Apigo, C. Prodan, A. Alù, E. Prodan, and A. B. Khanikaev, *Communications Physics* **2**, 55 (2019).
- [40] W. Cheng, E. Prodan, and C. Prodan, *Phys. Rev. Lett.* **125**, 224301 (2020).
- [41] Y. Xia, A. Erturk, and M. Ruzzene, *Phys. Rev. Applied* **13**, 014023 (2020).
- [42] Z.-G. Chen, W. Zhu, Y. Tan, L. Wang, and G. Ma, *Phys. Rev. X* **11**, 011016 (2021).
- [43] M. Gei, Z. Chen, F. Bosi, and L. Morini, *Applied Physics Letters* **116**, 241903 (2020), <https://doi.org/10.1063/5.0013528>.
- [44] L. Balents, C. R. Dean, D. K. Efetov, and A. F. Young, *Nat. Phys.* **16**, 725 (2020).
- [45] E. Y. Andrei and A. H. MacDonald, *Nature Materials* **19**, 1265 (2020).
- [46] Y.-Z. Chou, Y. Fu, J. H. Wilson, E. J. König, and J. H. Pixley, *Phys. Rev. B* **101**, 235121 (2020).
- [47] S. R. White, *Phys. Rev. Lett.* **69**, 2863 (1992).
- [48] U. Schollwöck, *Rev. Mod. Phys.* **77**, 259 (2005).
- [49] A. Szabó and U. Schneider, *Physical Review B* (2020), 10.1103/PhysRevB.101.014205, arXiv:1909.02048.
- [50] T. S. Gonçalves, M. Gonçalves, P. Ribeiro, and B. Amorim, “Topological phase transitions for any taste in 2d quasiperiodic systems,” (2022), arXiv:2212.08024 [cond-mat.dis-nn].
- [51] S. Iyer, V. Oganesyan, G. Refael, and D. A. Huse, *Phys. Rev. B* **87**, 134202 (2013).
- [52] R. Mondaini and M. Rigol, *Phys. Rev. A* **92**, 041601 (2015).
- [53] R. Modak and S. Mukerjee, *Phys. Rev. Lett.* **115**, 230401 (2015).
- [54] M. Lee, T. R. Look, S. P. Lim, and D. N. Sheng, *Phys. Rev. B* **96**, 075146 (2017).
- [55] M. Žnidarič and M. Ljubotina, *Proceedings of the National Academy of Sciences* **115**, 4595 (2018), <https://www.pnas.org/content/115/18/4595.full.pdf>.
- [56] S. Xu, X. Li, Y.-T. Hsu, B. Swingle, and S. Das Sarma, *Phys. Rev. Research* **1**, 032039 (2019).
- [57] E. V. H. Doggen and A. D. Mirlin, *Phys. Rev. B* **100**, 104203 (2019).
- [58] D. Vu, K. Huang, X. Li, and S. D. Sarma, “Fermionic many-body localization for random and quasiperiodic systems in the presence of short- and long-range interactions,” (2021), arXiv:2109.04489 [cond-mat.dis-nn].
- [59] A. S. Aramthottil, T. Chanda, P. Sierant, and J. Zakrzewski, *Phys. Rev. B* **104**, 214201 (2021).
- [60] Y. Wang, C. Cheng, X.-J. Liu, and D. Yu, *Phys. Rev. Lett.* **126**, 080602 (2021).
- [61] C. Schuster, R. A. Römer, and M. Schreiber, *Phys. Rev. B* **65**, 115114 (2002).
- [62] Y. E. Kraus, O. Zilberberg, and R. Berkovits, *Phys. Rev. B* **89**, 161106 (2014).
- [63] *SciPost Phys.* **1**, 010 (2016).
- [64] T. Cookmeyer, J. Motruk, and J. E. Moore, *Phys. Rev. B* **101**, 174203 (2020).
- [65] D. Vu and S. Das Sarma, *Phys. Rev. Lett.* **126**, 036803 (2021).
- [66] R. Oliveira, M. Gonçalves, P. Ribeiro, E. V. Castro, and B. Amorim, “Incommensurability-induced enhancement of superconductivity in one dimensional critical systems,” (2023), arXiv:2303.17656 [cond-mat.supr-con].
- [67] M. Gonçalves, J. H. Pixley, B. Amorim, E. V. Castro, and P. Ribeiro, “Short-range interactions are irrelevant at the quasiperiodic-driven luttinger liquid to anderson glass transition,” (2023), arXiv:2304.09197 [cond-mat.dis-nn].
- [68] A. Uri, S. C. de la Barrera, M. T. Randeria, D. Rodan-Legrain, T. Devakul, P. J. D. Crowley, N. Paul, K. Watanabe, T. Taniguchi, R. Lifshitz, L. Fu, R. C. Ashoori, and P. Jarillo-Herrero, “Superconductivity and strong interactions in a tunable moiré quasiperiodic crystal,” (2023), arXiv:2302.00686 [cond-mat.mes-hall].
- [69] F. Liu, S. Ghosh, and Y. D. Chong, *Phys. Rev. B* **91**, 014108 (2015).
- [70] M. A. Cazalilla, R. Citro, T. Giamarchi, E. Orignac, and M. Rigol, *Rev. Mod. Phys.* **83**, 1405 (2011).
- [71] See supplemental material for: the origin of the narrow band; the detailed finite-size scaling analysis; additional results for V_2 larger than 1 and for the comparison between commensurate and incommensurate systems; and results obtained by using twisted boundary conditions.
- [72] Y. Hatsugai and M. Kohmoto, *Phys. Rev. B* **42**, 8282 (1990).
- [73] J. H. Han, D. J. Thouless, H. Hiramoto, and M. Kohmoto, *Phys. Rev. B* **50**, 11365 (1994).
- [74] M. Fishman, S. R. White, and E. M. Stoudenmire, “The ITensor software library for tensor network calculations,” (2020), arXiv:2007.14822.
- [75] M. Fishman, S. R. White, and E. M. Stoudenmire, *CoRR abs/2007.14822* (2020), 2007.14822.
- [76] For the largest used system sizes, in some cases we slightly relaxed this criterium to $\Delta E_{GS} < 10^{-7}$, $\Delta_H < 5 \times 10^{-6}$ and $\Delta S_{GS} < 5 \times 10^{-4}$.
- [77] S.-J. GU, *International Journal of Modern Physics B* **24**, 4371 (2010), <https://doi.org/10.1142/S0217979210056335>.

Supplemental Material for:

Incommensurability-driven quasi-fractal order in 1D narrow-band moiré system

CONTENTS

Acknowledgments	7
References	7
S1. Origin of narrow-band	SM - 1
S2. Finite-size scalling analysis	SM - 2
S3. Additional results for $V_2 \geq 1$	SM - 4
S4. Commensurate vs. incommensurate: Additional results	SM - 5
S5. Results with twisted-boundary-conditions	SM - 7

S1. ORIGIN OF NARROW-BAND

To see how a narrow-band develops around $E = 0$ for the model in Eq. 1 in the non-interacting limit, we analyse the quasiperiodic hopping term in momentum space, which reads

$$H_0^{\text{qp}} = V_2 \sum_n \cos[2\pi\tau(n + 1/2) + \phi] c_n^\dagger c_{n+1} + \text{h.c.} \quad (\text{S1})$$

Making a Fourier transform in the electron operators,

$$c_n = \frac{1}{\sqrt{N}} \sum_k e^{ikn} c_k, \quad (\text{S2})$$

we have that

$$H_0^{\text{qp}} = \sum_k \cos(k + \pi\tau) [e^{i\phi} c_{k+2\pi\tau}^\dagger c_k + e^{-i\phi} c_k^\dagger c_{k+2\pi\tau}]. \quad (\text{S3})$$

From this calculation we see that the quasiperiodic hopping term couples Bloch momenta k and $k \pm 2\pi\tau n$ in n -th order perturbation theory. For small V_2 we can stick to first order and, setting $\tau = 1/2 + \epsilon$, momenta with $\Delta k = \pi \pm \epsilon$ will be coupled. As a consequence, gaps open at momenta separated by Δk , leaving a narrow-band around $E = 0$ that is flatter for smaller ϵ (and at the same time corresponds to a smaller portion of the spectrum), see Fig. S1.

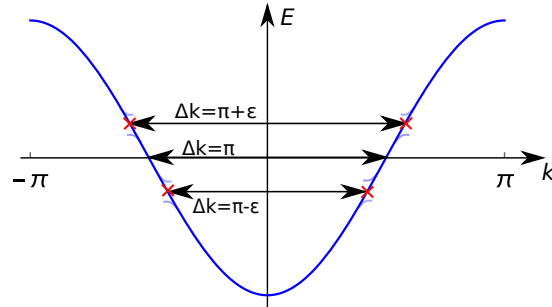


FIG. S1. Narrow-band formation: momenta separated by $\Delta k = \pi \pm \epsilon$ are coupled and gaps are opened, leaving a narrow-band around $E = 0$.

S2. FINITE-SIZE SCALLING ANALYSIS

In this section we provide details on how the critical points in the phase diagram in Fig. 1 were obtained. Using finite-size scaling analysis, we computed thermodynamic-limit extrapolations for several different quantities. Besides the charge gap, fidelity susceptibility and $\text{IPR}_\kappa(\langle \delta \mathbf{n} \rangle)$ shown in the main text, we also computed the entanglement entropy at the middle bond, S , and the quantity $\chi_R = N^{-1} \sum_i \langle \delta n_i \rangle^2$.

Below, we detail how the thermodynamic limit extrapolations were carried out for each quantity.

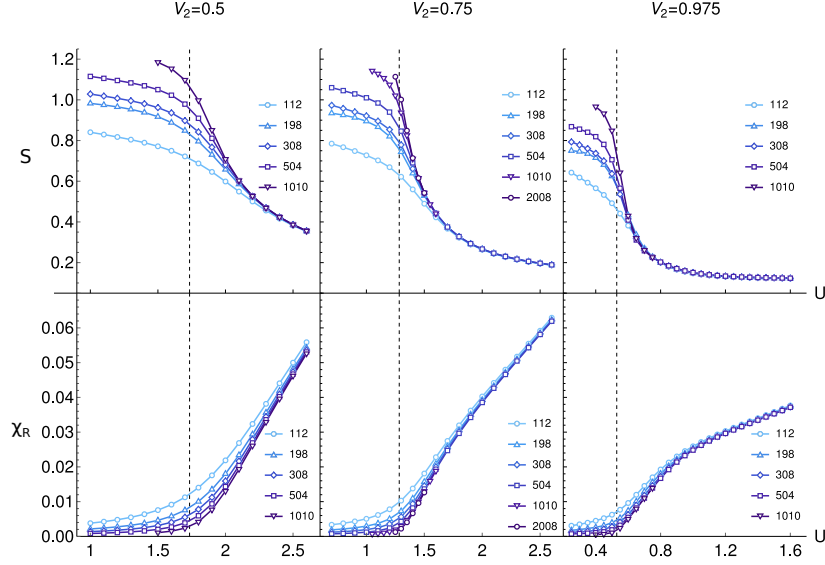


FIG. S2. Finite-size scaling results for (a) entanglement entropy at middle bond, S ; (b) $\chi_R = N^{-1} \sum_i \langle \delta n_i \rangle^2$. The top label indicates the value of V_2 used in the corresponding column, in (a,b). The dashed lines in each figure correspond to the thermodynamic limit extrapolation of the critical point, that we detail below.

Charge gap.— For large enough system and close to the phase transition, we assume that the charge gap obeys the scaling hypothesis

$$N\Delta_c(U, N) = N^a f(N^b [U - U_c]), \quad (\text{S4})$$

where $f(x)$ is a scaling function, a and b are some scaling exponents, and U_c is the critical interaction strength. Taking a logarithmic derivative of $N\Delta_c(U, N)$ with the system size we have that

$$\frac{d \log(N\Delta_c(U, N))}{d \log N} = a + \frac{f'(N^b [U - U_c])}{f(N^b [U - U_c])} N^b [U - U_c]. \quad (\text{S5})$$

From the above expression we see that at $U = U_c$, the above quantity becomes independent of the system size N , and by plotting it versus U the lines for different system sizes should cross. However, we have not used this criterion for the charge gap, for two reasons: (i) it provides a poor result for the $V_2 = 0$ case, for which the U_c is known, (ii) for some values of V_2 , there is no clear crossing point. So instead, we notice that by solving the condition

$$\frac{d \log(N\Delta_c(U, N))}{d \log N} = \lambda \quad (\text{S6})$$

as a function of U , for some fixed value λ close to 0, under the scaling hypothesis, this is equivalent to solving

$$a + \frac{f'(x_\lambda^*)}{f(x_\lambda^*)} x_\lambda^* = \lambda, \quad (\text{S7})$$

where $x_\lambda^* = N^b [U_\lambda^*(N) - U_c]$ and $U_\lambda^*(N)$ is the value of U such that the logarithmic derivative equals λ for a given system size. Therefore, under the scaling hypothesis we have

$$U_\lambda^*(N) = U_c + \frac{x_\lambda^*}{N^b}$$

and by determining U_λ^* for different system sizes and extrapolating it to $N \rightarrow \infty$, we can extract U_c . We numerically implemented this criterion as follows. For each U we make a linear fit of the $\log N \Delta_c$ data points as a function of $\log N$, excluding the smallest sizes up to when only two sizes remain. The slopes obtained by fitting each set of system sizes give rise to the data points $(U, \Lambda_{N_{\text{av}}})$, where $\Lambda_{N_{\text{av}}} = \left. \frac{d \log N \Delta_c}{d \log N} \right|_{N=N_{\text{av}}}$ and N_{av} is the average of the system sizes used to make the fit. These results are exemplified in Fig. S3(a-middle). In the next step we interpolate these points and check when the resulting curves cross a value λ that we choose close to 0 (in Fig. S3 we used $\lambda = 0.025$). The reason for this choice is that choosing $\lambda = 0$ gives a very accurate estimation of the well-known critical point $U_c = 2$ for $V_2 = 0$ ($U_c = 2.001 \pm 0.008$). We then extrapolate the value of U for which $\Lambda_{N_{\text{av}}} = \lambda$, that we label $U_\lambda^*(N)$, and plotted it as a function of N^{-1} , observed that the exponent $b \approx 1$ and extracted U_c by making a linear fit of $U_\lambda^*(N)$ vs N^{-1} . We notice that in this method, we cannot always choose $\lambda = 0$, since in some cases the $\Lambda_{N_{\text{av}}}$ curves do not cross this value.

χ_R .— For the quantity χ_R , we expect it to scale to zero with N in the LL phase (the fluctuations $\langle \delta n_i \rangle$ are non-extensive) and to converge to a constant in the CDW phase (due to extensive fluctuations). An example of this behaviour is shown in S2(b). We made the same scaling hypothesis for χ_R as for the charge gap and used an identical procedure to determine the logarithmic derivative of χ_R with respect to system size, $\Lambda_{N_{\text{av}}}^R = \left. \frac{d \log \chi_R}{d \log N} \right|_{N=N_{\text{av}}}$. To extrapolate to the thermodynamic limit, we used the criterion of the $\Lambda_{N_{\text{av}}}^R$ at the phase transition, by extracting crossing of the curves of $\Lambda_{N_{\text{av}}}^R$ vs U for different system sizes, as this was always well defined. An example is shown in Fig. S3(b).

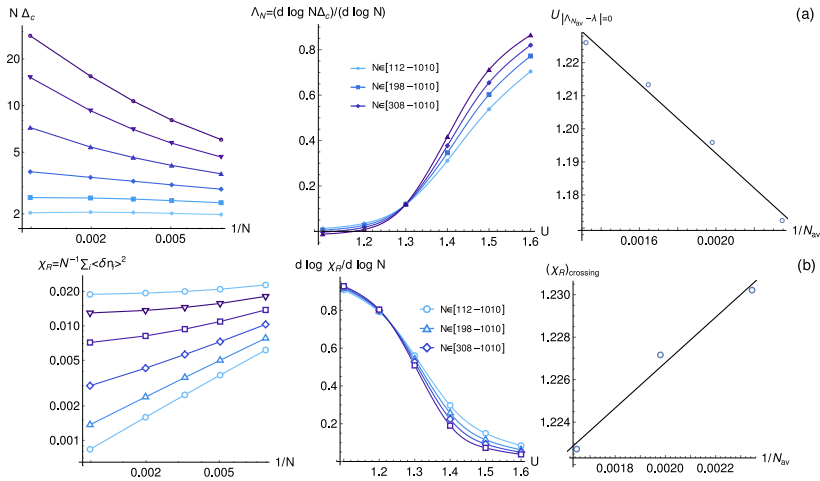


FIG. S3. Example of thermodynamic-limit extrapolations for the charge gap and χ_R , for $V_2 = 0.75$.

Fidelity susceptibility.— For χ_F we extrapolate the maximizant $U_c(N)$ using the 3 largest sizes and assuming $U_c(N) = U_c + \beta/N$.

Entanglement entropy.— In the case of the entanglement entropy, it increases with N in the LL phase, while it converges to a constant in the CDW phase, as illustrated in Fig. S3(a). For finite N , $|\partial S/\partial U|$ has a maximum at a value $U^*(L)$ that approaches the critical interaction strength U_c as N is increased. We extrapolated the maximizant of $|\partial S/\partial U(N)|$ using the 3 largest sizes, again assuming that $U^*(L) = U_c + \beta/N$.

$\text{IPR}_\kappa(\langle \delta \mathbf{n} \rangle)$.— For $\text{IPR}_\kappa(\langle \delta \mathbf{n} \rangle)$ we extrapolate the crossing point between the curves of consecutive system sizes, considering the crossings for the 5 largest system sizes. Extrapolations for these quantities are exemplified in Fig. S4, for $V_2 = 0.75$.

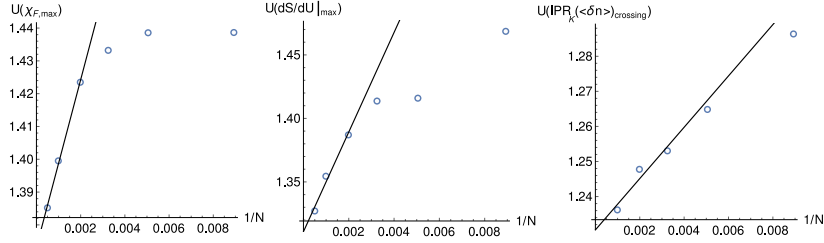


FIG. S4. Example of thermodynamic-limit extrapolations for χ_F , $dS/dU|_{\max}$ and $\text{IPR}_\kappa(\langle \delta \mathbf{n} \rangle)$, for $V_2 = 0.75$.

Finally, in Fig. S5, we show the calculations of the extrapolated critical points, for each different quantity, separately. We can see that for lower V_2 , the extrapolation using χ_F considerably overestimates the critical point comparing to the remaining quantities. This suggests that the finite-size effects are more severe for this quantity, in this regime. For $V_2 = 0.5$, we therefore estimate the critical point by averaging over all results, except for the χ_F extrapolation. On the other hand, for $V_2 \geq 0.75$ we average over all results to estimate the critical point.

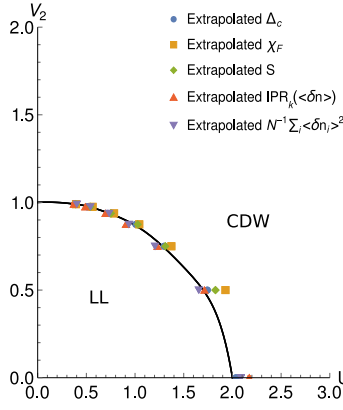


FIG. S5. Extrapolated critical points for the different quantities.

We finish this section by supporting the claim made in the main text that $U_c \sim (1 - V_2)^\mu$, with $\mu \approx 0.4$. The results are presented in Fig. S6.

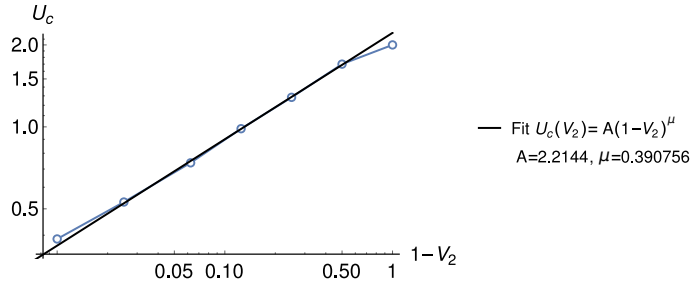


FIG. S6. Fit of $\log U_c$ vs. $\log(1 - V_2)$, using the 5 points with larger V_2 .

S3. ADDITIONAL RESULTS FOR $V_2 \geq 1$

In this section we present additional results inside the region $V_2 \geq 1$ of the phase diagram. In the main text we chose $V_2 = 3.5$, so that the convergence of the DMRG calculations was satisfactory down to $U = 0$ for the used system sizes. As we have seen there, for a given system size, the smallest charge gaps occur for smaller U , in which case a good enough convergence is more challenging to achieve. For $V_2 = 3.5$, however, we can achieve a good convergence even at $U = 0$, as can be seen in Fig. S7. In this figure we plot the exact and DMRG calculations of $\langle \delta n_i \rangle$ for $U = 0$ and for different system sizes and see that only for $N = 2008$ we start seeing more significant deviations.

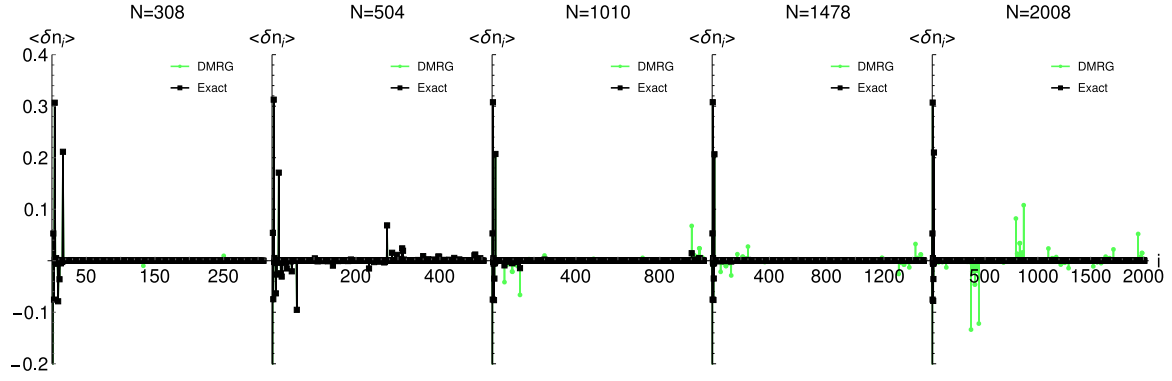


FIG. S7. Comparison of exact and DMRG calculations for $\langle \delta n_i \rangle$, for $U = 0, V_2 = 3.5, \phi = 1.8$ and different system sizes.

We also obtained results for other $V_2 \geq 1$. However, in this case it was not possible to converge the results down to $U = 0$ for sufficiently large system sizes. In Fig. S8 we show results for $V_2 = 1$ and $V_2 = 1.5$ only for $\Delta_c \geq 10^{-4}$, for which there was a very good agreement between the DMRG and exact results for $V_2 = 3.5$. In both cases, we see that χ_F has a maximum that saturates with system size, again pointing to a crossover instead of a true quantum phase transition. This is also corroborated by the S and $\text{IPR}_\kappa(\langle \delta \mathbf{n} \rangle)$ results: S also saturates with N and $\text{IPR}_\kappa(\langle \delta \mathbf{n} \rangle)$ does not decrease with N .

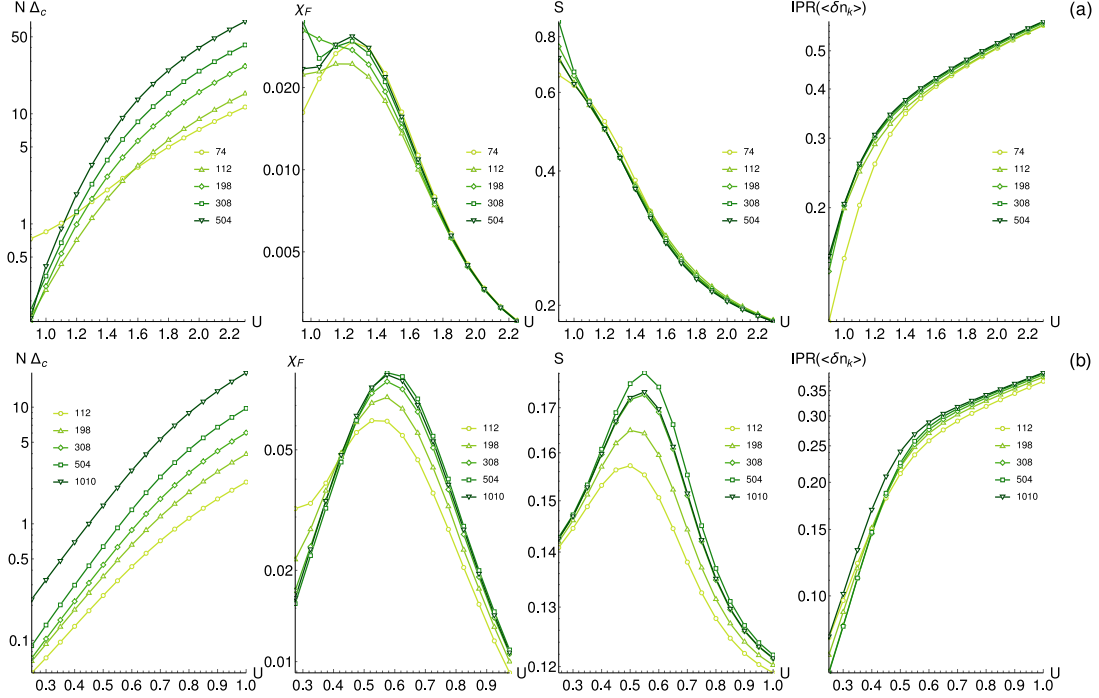


FIG. S8. Additional results for $V_2 = 1.5, \phi = 0.46$ (a) and $V_2 = 1, \phi = \pi/4$ (b).

S4. COMMENSURATE VS. INCOMMENSURATE: ADDITIONAL RESULTS

In this section we present some additional results with special focus on the comparison between commensurate (CS) and incommensurate systems (IS). For the CS, we take, as in the main text, a system with $\tau = 7/12$, having both the unit cell and the Moiré pattern with 12 sites. In the main text, we showed plots of $\langle \delta n_\kappa \rangle$ as a function of κ . In Fig. S9 we plot $|\langle \delta n_{\kappa_k} \rangle|$, with $\kappa_k = \pi + 2\pi\tau k$, as a function of k . This explicitly shows that CDW order is dominated by wave vectors with smaller $|k|$, as mentioned in the main text. Since for each approximant we have $\tau = p/N$ with

p and N co-primes, this operation is just a reshuffling of the values $\kappa_j = 2\pi j/N$, $j = 0, \dots, N-1$. For the CS, κ_j only takes 12 different values, indicating that the obtained CDW order has the same unit cell as the commensurate system.

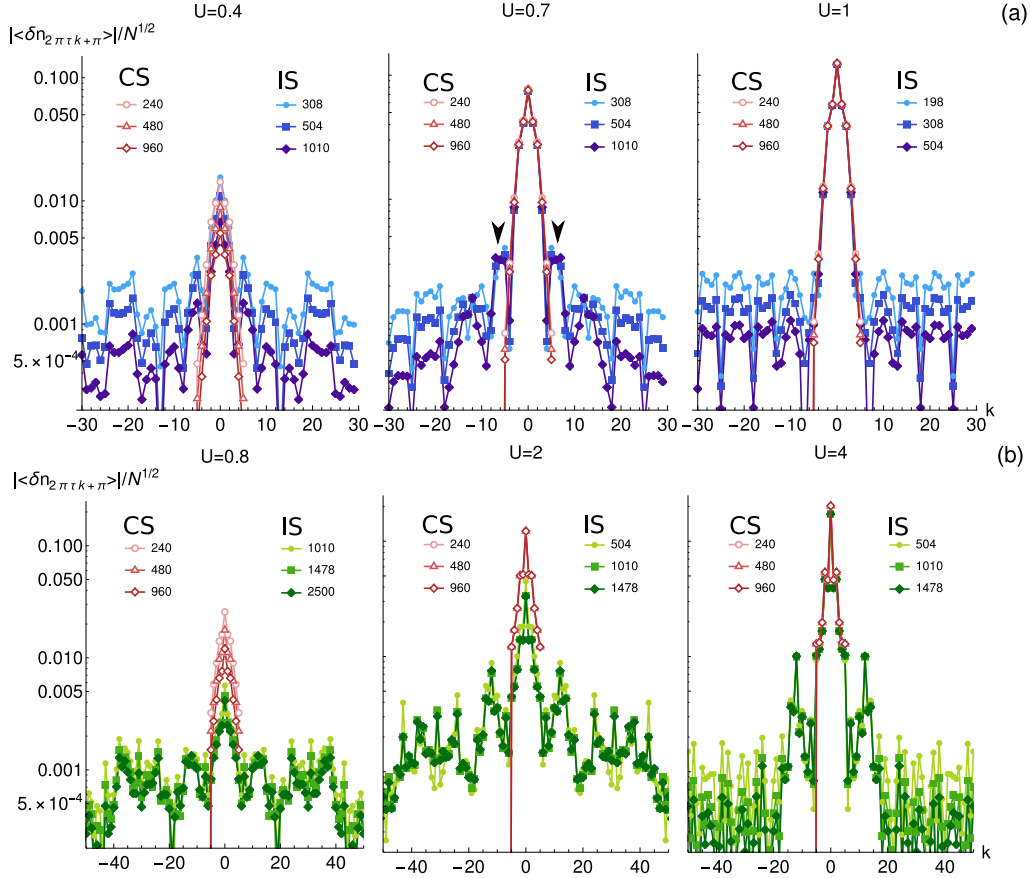


FIG. S9. $|\langle \delta n_{\kappa_k = \pi + 2\pi\tau k} \rangle|/\sqrt{N}$ for CS and IS, for $V_2 = 0.975$ (a) and $V_2 = 3.5$ (b). For the CS we used $\tau = \tau_c = 7/12$ and $\phi = 0$. In this case, there are only 12 inequivalent κ_k . For the IS we used $\phi = \pi/4$ in (a) and $\phi = 1.8$ in (b). The arrows in (a) indicate ordered peaks that exist for the IS and that are absent for the CS. For $V_2 = 3.5$, in (b), we see that for smaller U - left and middle panels - the type of order is completely different for the IS and CS - in the former case there are converged peaks up to very large $|k|$, while in the latter $|k|$ is bounded and the ordered phase breaks down at sufficiently small U .

As we mentioned in the main text, depending on the choice of ϕ , an energy gap can open for the CS around $E = 0$ in the non-interacting limit. We show this in Fig. S10, where we plot the energy bands around $E = 0$ constituting the narrow-band as a function of Bloch momentum κ and $\varphi = 12\phi$ (the energy bands have a periodicity in ϕ of $\Delta\phi = \pi/6$). In this figure, we can see that even for $V_2 < 1$, a small energy gap can open. In fact, the system is only truly gapless for $\phi = \pi j/6$, $j \in \mathbb{Z}$. For this reason, we chose $\phi = 0$ for the results in the main text so that the non-interacting limit is gapless both in the commensurate and in the incommensurate cases.

One can also ask what happens if ϕ is chosen so that the CS is gapped in the non-interacting limit. We observed that a phase transition also occurs, but in this case between gapped disordered and gapped CDW phases. Example results are shown in Fig. S11 (top panel) for $V_2 = 1.25$ and $\phi = \pi/4$ in which case the CS is gapped for $U = 0$; and, for comparison, for $V_2 = 1.25$ and $\phi = 0$, in which case the CS is gapless CS [Fig. S11 (bottom panel)]. We can see that the critical U is larger in the gapped case. However, while the entanglement entropy at the middle bond, S , increases with system size in the small- U phase of the gapless CS [Fig. S11 (c-bottom)] - as it should in a LL phase - it saturates for the gapped CS, only diverging at the critical point [Fig. S11 (c-top)]. The gapped phase is therefore stable to finite interactions, up to a considerably large critical U at which the transition into the commensurate CDW takes place.

Finally, in the main text we have mentioned that for $V_2 \geq 1$ there are fine-tuned values of V_2 for which some hoppings vanish and that in these cases, the narrow-band becomes completely flat. These calculations are shown explicitly in Fig. S12.

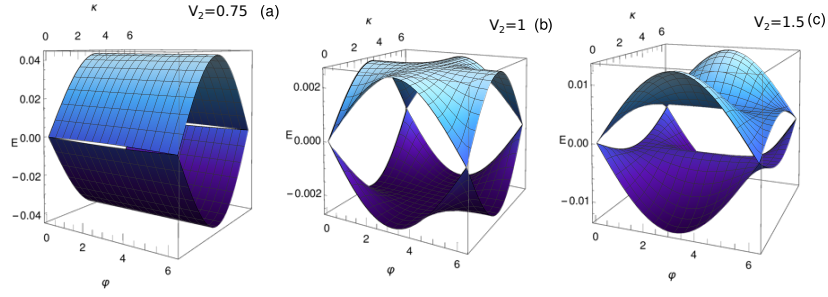


FIG. S10. Dispersion of energy bands around $E = 0$ for the CS with $\tau = 7/12$ as function of the Bloch momentum κ and $\varphi = 12\phi$.

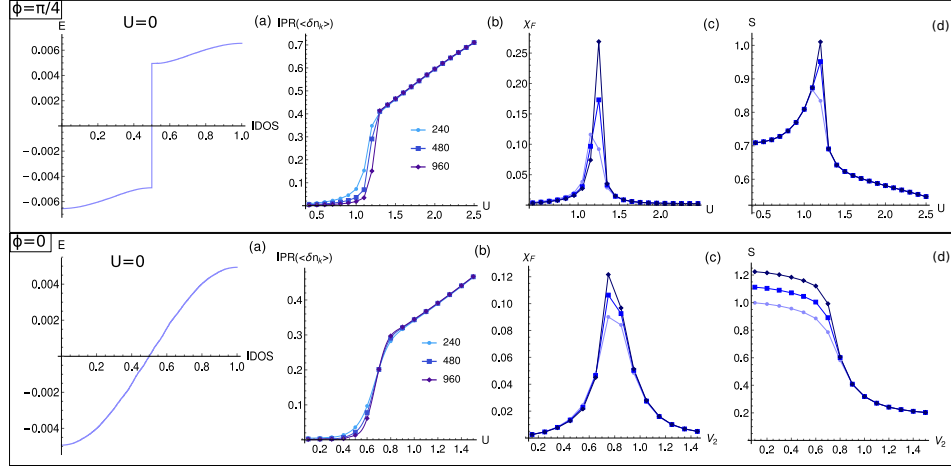


FIG. S11. (a) IDOS for the CS with $\tau = 7/12$, for $U = 0, V_2 = 1.25$ and $\phi = \pi/4$, gapped CS (top); $\phi = 0$, gapless CS (bottom). (b-d): DMRG results for the same parameters as in (a), for variable U , in the gapped (top) and gapless (bottom) cases.

S5. RESULTS WITH TWISTED-BOUNDARY-CONDITIONS

In this section, we complement the results of the main text obtained with OBC, by studying a system with twisted boundary conditions (TBC). In this case, the system sizes that we can reach are significantly smaller than for OBC. Nonetheless, the aim of this section is corroborate the results obtained for OBC whenever possible. In the results that follow, we take $\tau = \{27/46, 43/74, 65/112\}$, choosing the fraction's denominator as the system size. TBC are applied in the Hamiltonian as

$$H = \sum_{j=0}^{N-2} t_j c_j^\dagger c_{j+1} + e^{i\kappa} t_{N-1} c_{N-1}^\dagger c_0 + \text{h.c.} + U \sum_j n_j n_{j+1} \quad , \quad (\text{S8})$$

where κ is the phase twist and again $t_j = -(1 + V_2 \cos[2\pi\tau(j + 1/2) + \phi])$. Below we present results for different configurations of ϕ and κ .

We start by presenting results for the entanglement entropy at the middle bond, S , in Fig. S13. The latter should converge to a constant in the CDW phase, while increasing with system size in the LL phase. There are still strong finite-size effects that do not allow us to see the saturation of S in the CDW phase close to the critical point [Figs. S13(a,b)]. Nonetheless, S develops a maximum at a value of U that does not depend very significantly on N and that very accurately matches the critical point computed using OBC [see Fig. S13(c)]. For $V_2 \geq 1$, finite-size effects become too severe to explore the small U regime.

Most importantly, in order to verify the type of order in the CDW phase, we also compute the structure factor $S(q)$ defined as

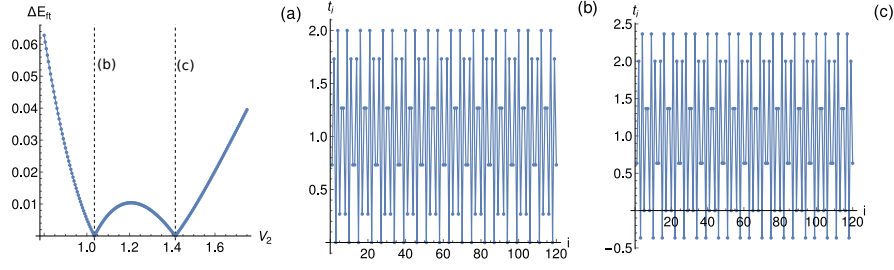


FIG. S12. (a) Narrow-band width, ΔE_{ft} , in the non-interacting limit, for the CS with for $\tau = 7/12$ and $\phi = 0$, as a function of V_2 . (b,c) Hopping configurations at the values of V_2 signaled by the dashed lines in (a). We can see that the narrow-band becomes completely flat when hoppings vanish exactly.

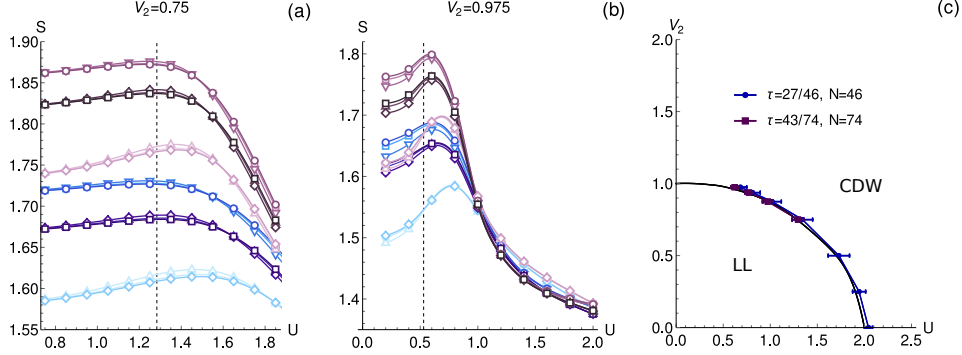


FIG. S13. (a,b) Entanglement entropy at the middle bond, S , as a function of U for $N = 46$ (blue) and $N = 74$ (purple) and for $V_2 = 0.75$ (a) and $V_2 = 0.975$ (b). The dashed lines indicate the critical point computed using open boundary conditions. The different tones correspond to different configurations of ϕ and κ . We used a grid of configurations $\Phi_{i+N_\kappa j} = (\phi_i, \kappa_j) = \left(\frac{\pi}{2N} + \frac{2\pi i}{N_\phi}, \frac{\pi}{2} + \frac{2\pi j}{N_\kappa}\right)$, $i = 0, \dots, N_\phi - 1$; $j = 0, \dots, N_\kappa - 1$, where $N_\phi \times N_\kappa = 3 \times 3$ is the total number of configurations. The lighter (darker) color correspond to the Φ_0 (Φ_8) configuration. (c) Maximizants of S , averaged over all the 9 configurations along with the interpolation of the critical line obtained using open boundary conditions (full black line). The standard deviation is indicated by the error bars.

$$S(q) = \frac{1}{N} \sum_{i=1}^N \sum_{j=1}^N [\langle n_i n_j \rangle - \langle n_i \rangle \langle n_j \rangle] e^{iq(i-j)} \quad (\text{S9})$$

Order at $q = q_0$ is signaled by a diverging $S(q_0)$ with N : in the thermodynamic limit, $S(q_0)/N$ should be finite in this case, otherwise it should scale to zero. In Fig. S14, we present results for $V_2 = 0.975$ and $V_2 = 1.75$ for U within the CDW phase. There we see that $S(q)$ only increases with N at $q_n = \pi + 2\pi\tau(n-1)$, the wave-vectors at which we have seen the development of order using OBC. However, finite-size effects are much stronger for TBC (due to the smaller available sizes) and it becomes challenging to capture the divergence of $S(q_n)$ for $n > 4$. Based on the results obtained for OBC, we conjecture that for large enough system sizes, the quasi-fractal regime should be signaled by the divergence of $S(q_n)$ up to large order in n .

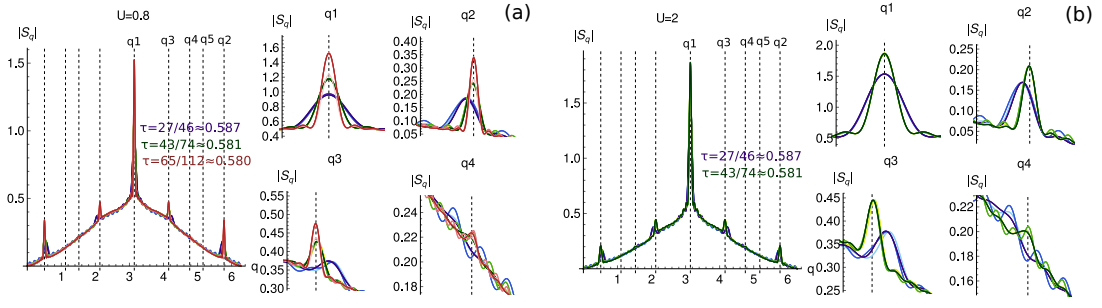


FIG. S14. Structure factor S_q , defined in Eq. S9 for $V_2 = 0.975, U = 0.8$ (a) and $V_2 = 1.75, U = 2$ (b). Curves with different lightness were obtained for different configurations of ϕ and κ . The dashed lines are located at $q_n = \pi + 2\pi\tau(n-1)$. The right smaller panels correspond to zoom-ins around q_n up to $n = 4$.